Composite Structures 308 (2023) 116674

Contents lists available at ScienceDirect

Composite Structures

journal homepage: www.elsevier.com/locate/compstruct

The influence of the manufacturing process and test boundary conditions on the buckling load of thin-walled cylindrical CFRP shells

Tobias S. Hartwich [a,*], Stefan Panek [a], Dirk Wilckens [b], Matthias Bock [b], Dieter Krause [a]

[a] TUHH, Institute of Product Development and Mechanical Engineering Design, Hamburg, Germany
[b] DLR, Institute of Composite Structures and Adaptive Systems, Braunschweig, Germany

ARTICLE INFO

Keywords:
Buckling
Composite shells
Imperfections
Test rig

ABSTRACT

Thin-walled cylindrical CFRP shells tend to buckle under compressive loads. The experimental buckling load is significantly lower than the theoretical one. The reason for this are various kinds of imperfections which are partially caused by the manufacturing process and the test conditions. A major challenge in the design of these shells is the lack of experimental data. Additionally, the quality of test results is rarely critically reviewed in the validation of design approaches. In this paper, the influence of two different manufacturing processes on the geometric imperfections and the influence of three different test rigs on the buckling load are investigated in an experimental campaign with 12 cylindrical CFRP shells. Furthermore, the influence of varying the test rig boundary conditions is analysed.

1. Introduction

Thin-walled cylindrical shells are commonly used structures in aerospace engineering. Their behaviour under compressive load has been an intensive part of research for several decades. The main challenge in designing these structures is the large discrepancy between theoretical and experimental buckling loads [1]. With the use of orthotropic materials such as fibre plastic composites, new challenges have occurred. The approaches developed on isotropic cylinders lead to very conservative results (e.g. [2–5] or [6]).

One of the most common and established design approaches is the NASA SP-8007 [7]. This guideline suggests different ways to calculate a global knockdown factor which considers all imperfections and uncertainties. However, it often leads to very conservative design loads [4, 8]. Another well discussed approach is the Single Perturbation Load Approach (SPLA) [3] which is based on the idea that global buckling starts with an initial local buckle. However, in some configurations this approach does not lead to conservative designs [9]. Since most imperfections are of a stochastic nature, it is reasonable to consider probabilistic methods for the design of thin-walled cylinder shells. First approaches were developed by Bolotin in the 1960s [10], which have been further refined since then. Nevertheless, the required distributions of the influence parameters are often not available to the necessary extent and have to be assumed.

A major challenge is the range of influencing factors. Although the most common influencing factors are well known, there is a lack of profoundly documented published data. Most prominent are the geometric imperfections or so-called traditional imperfections [11], which are commonly described through Fourier coefficients [2,6,7]. In addition, there are the non-traditional imperfections [11] like load deviation or so-called load imperfections, scattering of material parameters or boundary conditions [7]. In this contribution, load imperfections are defined to include any deviation in loading from a uniform uniaxial stress state, particularly lateral loads and tilting of the shells.

A good summary of the existing database is given in [5,12]. In most cases, the data given is not complete or only small sample sizes are investigated. The development of new design approaches is often based on or validated using the results of such experiments. However, the testing conditions are rarely critically reviewed. The test rig boundary conditions are often unvaried, so the effect cannot be quantified. In literature it is commonly mentioned that the stiffness of the test rig has no influence on the buckling load [1]. However, it does have an influence on the post-buckling behaviour [1]. Only a few test rig comparisons have been carried out in literature (e.g. [13–15]). In a study of Meyer-Piening et al. [13] eight cylinders with different layups were tested on the DLR buckling test facility and a universal testing facility of EMPA. The difference of buckling loads was between 0.5% and 9.9%. In [14], three nominally identical cylinders were analysed on an in-house designed test rig and an MTS test facility. The buckling loads differ from -9.6 % to 15.2% between test rigs. Franzoni et al. [15] did a test rig comparison and found a difference of 22.3% in the buckling load. However, the cylinder collapsed in the second test rig.

---

* Corresponding author.
E-mail address: tobias.hartwich@tuhh.de (T.S. Hartwich).

https://doi.org/10.1016/j.compstruct.2023.116674
Received 20 October 2022; Received in revised form 2 December 2022; Accepted 3 January 2023

Hence, the range of buckling loads between these test rigs is comparable with the scatter of buckling loads induced by other influencing factors such as geometric imperfections. Many tests are carried out on special buckling benches, such as in [4,16–18]. But often, modified universal testing machines (UTM) are utilised (e.g. [19–21]). Therefore, the test rig influence should be analysed further to improve the validation of current and future design approaches.

It has been shown that the manufacturing process has an influence on the buckling load, as demonstrated by Hipp and Jensen [22] on the example of layer crossings caused by the winding process which can lead to local buckling effects.

To further investigate the influence of the manufacturing process and the test rig, twelve nominally identical cylindrical shells are tested and analysed in this publication. Six of these twelve cylinders were produced using the same manufacturing process. The cylinders are tested on three different test rigs under various boundary conditions. The influence of the manufacturing process on geometric imperfections and how they affect the buckling load is investigated. In addition, the influence of test rig boundary conditions on load deviations and their influence on the buckling load is evaluated. Finally, different design approaches are applied to the investigated shells and the results are compared with experimental values. For this exemplary comparison, the previously described NASA SP-8007 and SPLA, as well as the Linear Buckling Mode Imperfection approach (LBMI) from [23] and the Semi-Analytical Probabilistic procedure (SAP) from [24] are chosen. Hereby it is shown to what extent different manufacturing procedures and test rig boundary conditions are considered by the investigated design approaches.

2. Manufacturing process and test setup

2.1. Manufacturing process

The presented twelve cylinders were manufactured in three batches at the German Aerospace Center (DLR) in Braunschweig. The first and the second set consist of three cylinders each and are build layer by layer in a semi-automatic hand lay-up process. The third set containing six cylinders is produced in a winding process. Pre-impregnated carbon fibres (prepregs) are commonly used in manufacturing lightweight components. Slittapes are about 1/4″ broad unidirectional prepregs, which are used in winding or fibre placement technology. An AS7/8552 slittape was chosen as the fibre matrix system, which is placed on a rotating core at a specified speed and in a predefined winding pattern. The fibre material is on a storage carriage, which moves relative to the winding core. The direction and movement speed of the guide carriage in relation to the winding core rotation determine the laying direction of the fibres. The nominal inside diameter of all shells is 230 mm and the nominal length is 255 mm. A balanced quasi-isotropic layer structure with six layers was selected. This layup and material are chosen to achieve better comparability with [8]. In Table 1 all further geometric specifications are given. All cylinders have nominally identical properties to the ones investigated by Schillo in [8]. Due to the crossing sections induced by the winding process, the existing layer stack of the winded cylinders deviates from the nominal one for the ±30° layers. For the layered cylinders, it is not possible to realise a symmetrical layer stack, because it is not feasible to lay two identical orientations on top of each other without lifting the lower one. For all cylinders, the fibre angles of the 90° layers deviate by 0.5° due to the manufacturing process, as a 1/4″ pitch is covered during winding.

To determine the geometric imperfections, the cylinders are measured with an ATOS measuring system. The cylinders of the first and second set are measured before and after clamping in the fixture required for testing. A preliminary study in [25] shows that clamping only reduces long-wave circumferential imperfection modes, which have a negligible effect on the buckling load. Therefore, only the clamped cylinders are measured from the third set.

2.2. Test setup

In order to analyse the influence of the test setup, three different test rigs are used. Furthermore, on two of them the boundary conditions are varied. The boundary condition in a strict sense is a clamped connection for all shells, as both edges of the cylinders are supported by a steel fixture and held in an epoxy potting throughout all experiments. In the context of this study, the test rig boundary conditions describing the connection between the steel fixtures and the test rig itself are considered as boundary conditions in a broader sense. The first test rig is the Hexapod at TUHH which is a platform that can be moved through six degrees of freedom and is actuated by six hydraulic cylinders [26]. In the application used here, the cylinders are located in the lower test space where force is applied by lowering the platform as described in [25]. The CFRP cylinders are clamped in the fixtures developed by Schillo [8]. With these, the shells are mounted on a 6-DoF load cell. Deformation and strain of the cylinders are measured via three optical displacement sensors and six strain gauges. The radial arrangement makes it possible to determine the tilt angle of the upper shell edge. Fig. 1 shows a schematic of this test setup. There are two ways to connect the cylinder to the test platform. The first option is a fixed connection. Here, the upper clamping is screwed to the Hexapod test platform in a force-free manner via an adapter. This configuration allows the best comparability with most test setups found in literature. It has been further developed in comparison to Schillo's experiments. Alternately, a so-called simply supported connection, consisting of a ball joint for central load introduction while allowing the cylinder to tilt freely is used. In all tests, the load is applied in a displacement-controlled manner at a nominal speed of 1.5 mm/min.

The second test rig utilised is the well-known buckling facility of the Institute of Composite Structures and Adaptive Systems of DLR (Fig. 2). Test shells are located between the load distributor that is connected to an axially supporting top plate through three load cells and a lower drive plate. The top plate can be moved in vertical direction on three spindle columns to adapt the test device to the actual test article length.

A thin epoxy concrete layer consisting of epoxy reinforced with a mixture of sand and quartz powder is applied between both end plates of the test specimens and the adjacent parts of the test device, i.e. the drive plate and the load distributor. This procedure is done to ensure uniform load introduction on the test structure during loading. To investigate the influence of this addition to the setup, some buckling tests are also done without this epoxy layer. In the present test setup, adapter plates made of aluminium (Fig. 2) are used to overcome an incompatibility of the fixtures in which the cylindrical shells are potted. This is necessary since these plates are designed specifically for the interface of the Hexapod. However, the adapter plates are machined and as even as the adjacent parts of the buckling test facility. Thus, it is assumed that no further load deviations are introduced.

Axial loads and displacements are recorded during the tests. The reaction forces are measured by three 100-kN-load cells. The axial displacement is extracted by three displacement transducers, fixed between the load distributor and the axial drive and placed around the test specimen at 90°, 180° and 270°. The axial compression load is applied displacement controlled. Before the first buckling occurs, the load is applied stepwise until buckling and unloaded after 5 s in the early post buckling regime in order to avoid damaging the structure.

The third test rig used is a modified Galdabini Quasar 100 universal testing machine. In Fig. 3 an illustration of the test setup is shown. The clamped cylinder is mounted via an adapter plate on a 3-DoF load cell. The cylinder clamping can be centred on this adapter plate via four circumferentially positioned fine-thread screws. At the upper clamping, the cylinder is connected to the machine's crosshead via an adapter. The mounting is done force-free. As within the Hexapod test setup, displacements and strains are recorded by three optical displacement sensors and six strain gauges, respectively. The load is applied displacement controlled at a speed of 0.5 mm/min.

Table 1
Geometric specification of the cylinders.

	Set 1: Z1L1 - Z3L1	Set 2: Z1L2 - Z3L2	Set 3: Z1W2 - Z6W2
Nominal radius [mm]	115	115	115
Total length [mm]	255	255	255
Free length [mm]	215	215	215
Nominal R/t-Ratio	147	147	147
Fibre/Matrix	$AS7/8552$	$AS7/8552$	$AS7/8552$
Laminat layup	$[90^\circ, -30^\circ, 30^\circ, -30^\circ, 30^\circ, 90^\circ]$	$[90^\circ, -30^\circ, 30^\circ, -30^\circ, 30^\circ, 90^\circ]$	$[90^\circ, -30^\circ, 30^\circ]s$
Fabrication process	$laid\ layer\ by\ layer$	$laid\ layer\ by\ layer$	$filament - winding$

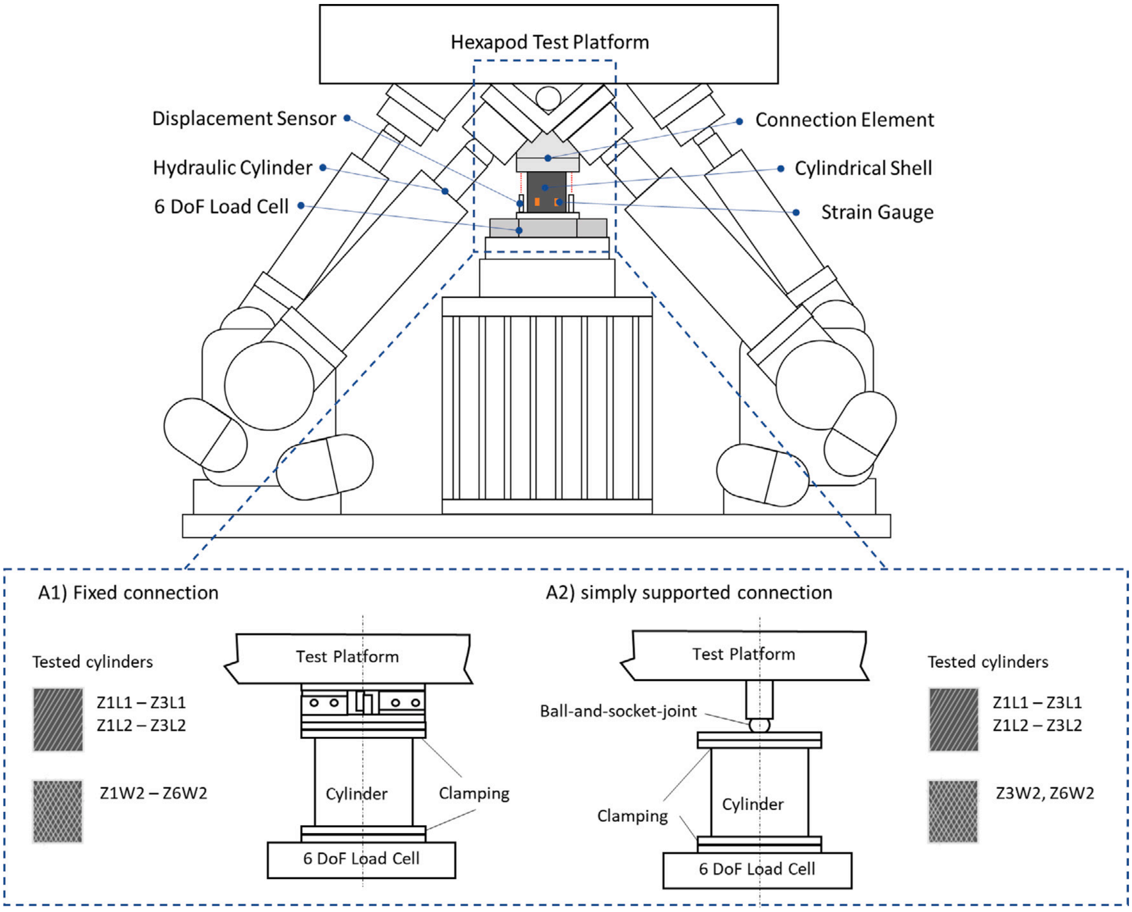

Fig. 1. Schematic illustration of the test setup on the Hexapod of the TUHH with the different boundary conditions, fixed (A1), simply supported (A2).

To determine the test rig influences, the cylinders are tested successively on different test rigs in different configurations. Table 2 shows the test design and the sequence of tests. The cylinders of the first two sets are first tested on the Hexapod with the fixed and then with the simple connection. This order is chosen because the simple connection permits significantly larger tilting angles in the post-buckling regime, which can lead to degradation. Comparisons between the Hexapod and the DLR buckling facility are carried out exclusively on the third set. Some shells are tested first on the Hexapod, others first on the DLR buckling bench. Furthermore, two cylinders of this set are also tested with the simple connection on the Hexapod in order to determine a possible interaction between boundary condition and manufacturing process. These can no longer be tested on the DLR buckling machine due to possible degradation. In addition, one layered and one wound cylinder are tested on a universal testing machine as well. The tests are carried out after all other experiments, as the test rig influence on degradation is not predictable. In order to trace a possible directional dependency of occurring lateral forces back to the test rig or production, the cylinders Z2L2 and Z3L2 are mounted rotated by 120° and 180° on the Hexapod.

2.3. Numerical analysis

In order to better quantify the influence of individual factors on the buckling load, FE simulations are conducted. These are done in Abaqus/Standard using the implicit solver with artificial damping. The nonlinear analyses to find buckling loads are run in a load-controlled manner. Estimating the buckling loads of the perfect shells is done through linear Eigenvalue analyses. The model is composed of S4R shell elements. Based on a convergence study [8], a mesh size of 215 × 722 elements is used. The bottom edge of the cylinder is considered fixed, while the top of the cylinder is modelled according to the existing boundary conditions. Geometric imperfections are mapped onto the nodes via Fourier decomposition in the form of the corresponding waves. The material parameters are calculated based on tensile tests from [27]. Since the fibres are loaded in compression, the Young's modulus in fibre direction will differ from the one under tension. As no material parameters for compressive loads are given by the manufacturer for AS7/8552, the ratio of compressive to tensile stiffness of two similar fibres with 8552 matrix is considered. For both AS4/8552 and IM7/8552 this ratio is 0.91 [28]. To estimate the compressive

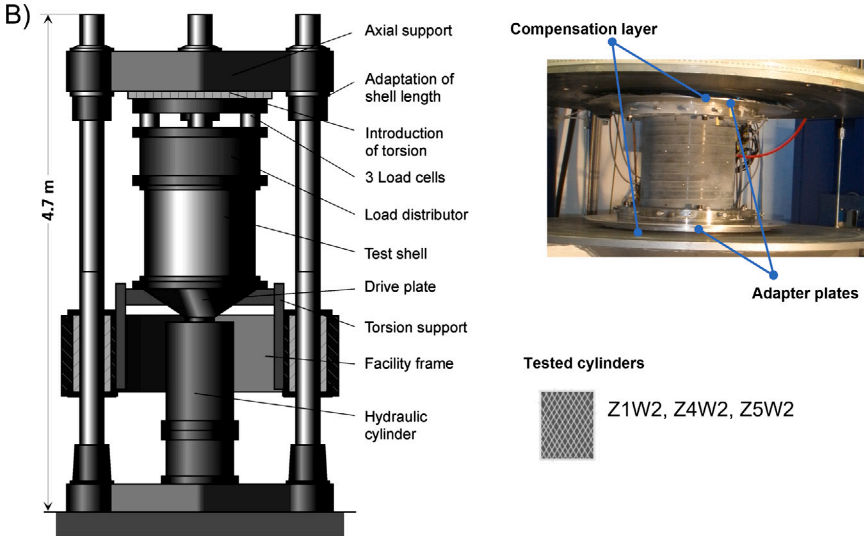

Fig. 2. Test setup of the DLR buckling facility.

Table 2
Test design of the buckling test, order of the used test rigs for each cylinder.

	Z1L1	Z2L1	Z3L1	Z1L2	Z2L2	Z3L2	Z1W2	Z2W2	Z3W2	Z4W2	Z5W2	Z6W2
Hexapod fixed (A1)	x	x	x	x	x	x		x	x	x	x	x
Hexapod simply supported (A2)	x	x	x	x	x	x			x			x
DLR buckling test facility (B1)							x			x	x	
DLR buckling test facility Without epoxy layer (B2)							x					
Hexapod fixed (A1)							x					
Galdabini UTM (C)				x				x				

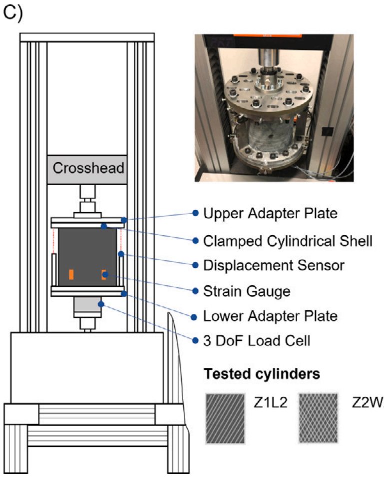

Fig. 3. Schematic illustration of the test setup of the modified universal testing machine.

stiffness, the tensile one is scaled by this factor which corresponds to a usual compression–tension stiffness ratio of carbon fibre reinforced plastics [4]. Finally, the material parameters are calculated using the equations from [29]. The present fibre volume fraction is estimated based on the respective shell thickness and the material properties are scaled accordingly using the classic composition rule and the corrected composition rule.

In first numerical investigations, the influence of manufacturing-specific geometric imperfection patterns is analysed. For this purpose, shells with a layer structure of [90°, −30°, +30°]s, [90°, −30°, +30°, −30°, +30°, 90°], [90°, +30°, −30°]s and [90°, +30°, −30°, +30°, −30°, 90°] are generated each. The material parameters are calculated based on the results from [27] and are given in Table 3. The values are then scaled, as described above, to the layer thickness which is assumed for all shells to be 0.125 mm for better comparability. All existing imperfection patterns are mapped onto each of the four cylinders and their buckling load is compared with that of a perfect shell. In a second numerical study, buckling loads are calculated for the cylinders using their respective geometric imperfections, wall thicknesses, resulting material parameters and load imperfections. Thereby, it is quantified to what extent the different factors affect the buckling load.

Finally, four design approaches are applied to the investigated shells. Following the procedure of NASA SP-8007 [7], the design load is calculated using nominal data from Table 1 and material properties from Table 3. The SPLA is carried out for the nominal geometry and for the measured wall-thicknesses with accordingly scaled material properties. For the LBMI approach the recommendations of [30] are followed to apply the first eigenmode of a shell as imperfection pattern to a perfect cylinder. As for the previous approaches, nominal geometry and material properties are assumed. The imperfection amplitude ξ [23] is chosen for the layered and wound cylinders separately, first approximating the average deviation from the nominal radius, then to represent the worst measured imperfection shape of each batch. With all three approaches design loads are calculated for all occurring stacking sequences of the ±30° layers. The SAP is carried out for the three sets separately, to better represent the differing underlying distributions of different parameters. Geometric imperfections and wall-thickness are grouped by manufacturing process. For simplicity, it is assumed that lateral forces and tilting of the upper clamping are independent of each other and that the direction follows a uniform distribution in the interval $[-\pi, \pi)$ for both kinds of load imperfection. While in reality a correlation of layer-thickness and stiffness properties is to be expected [29,31], there are not enough data available from [27] to make a well-founded estimation for the material considered in this study.

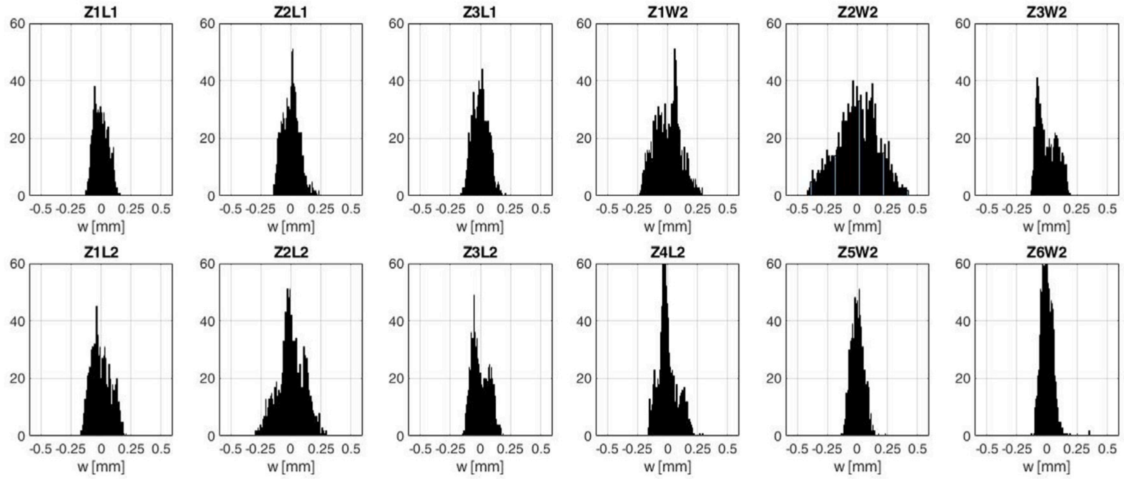

Fig. 4. Histogramms of the geometric imperfections of the analysed cylinders.

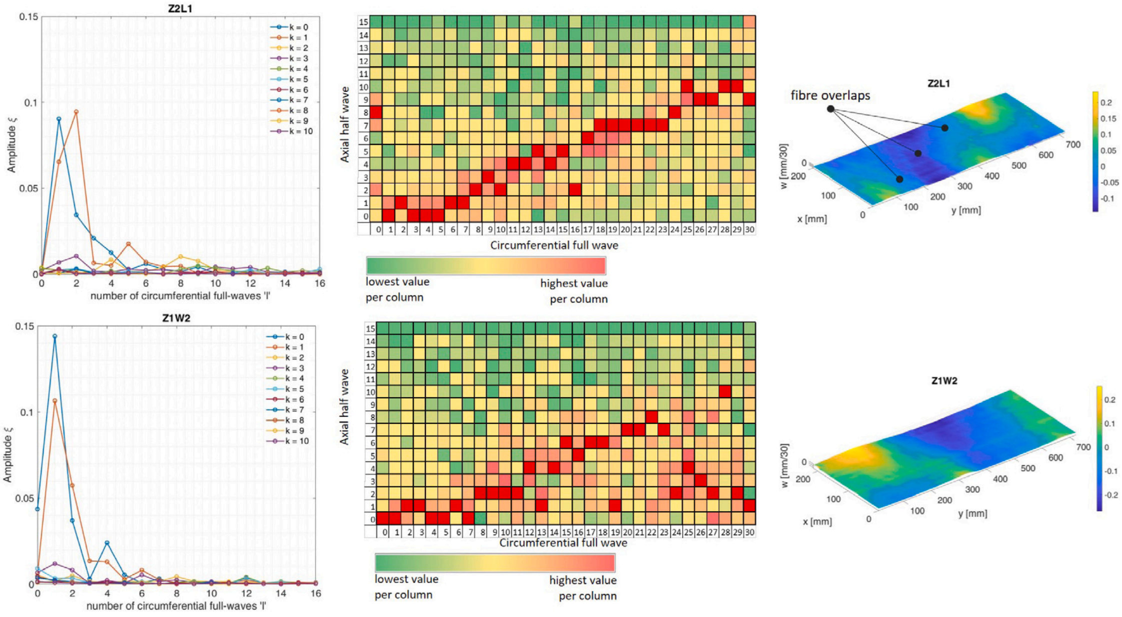

Fig. 5. Fourier coefficients and winding-up pattern of Z2L1 and Z1W2.

Table 3
Material properties.

	Values calculated based on [27]
t_{layer} [mm]	0.14
φ_f [%]	53.3
E_{11} (tension) [MPa]	137,640
E_{11} (compression) [MPa]	126,630
E_{22} [MPa]	10,230
G_{12} [MPa]	3640
ν_{12} [–]	0.32

3. Test results

3.1. Geometric imperfections

The optical measurement data are used to calculate the cylinder radius and, if measurement data from the inside of the shell are available, the wall thickness. In Table 4 the geometric specifications are shown. The outside cylinder radii of the first two sets are on average 114.72 mm, those of the third set 114.80 mm. This difference in radius is primarily due to different wall thicknesses. With a wall thickness of 0.70 mm to 0.72 mm, the layered cylinders are significantly thinner than the wound ones. Among the layered shells, those of the first set are slightly thinner. Of the third set, only Z2W2 was optically measured unclamped, so that the wall thickness is only determined for this shell, yielding a value of 0.82 mm. Since all cylinders were manufactured on the same winding mandrel, the difference between wall thicknesses and radii can be used to estimate an average inner radius of 114 mm for the remaining shells. This is then subtracted from the outside radius to approximate the wall thickness. The scatter of form deviations can be quantified via the standard deviation of the radii. As illustrated in Fig. 4, only cylinder Z2W2 has particularly large form deviations or geometric imperfections.

To further analyse the geometric imperfections and for use in FE-modelling, the optical measurement data are Fourier-transformed. Additionally, so-called wind-up patterns of the cylinder surfaces are examined. The peel-ply textures are visible on all cylinders. The winding-up patterns of shells from the first two sets show occasional fibre overlaps, as illustrated on Z2L1 in Fig. 5. Generally, the imperfection patterns of

Table 4
Measured geometric specification of the cylinders.

	Z1L1	Z2L1	Z3L1	Z1L2	Z2L2	Z3L2
Radius [mm]	114.72 ± 0.06	114.70 ± 0.07	114.71 ± 0.06	114.73 ± 0.08	114.72 ± 0.11	114.72 ± 0.07
Imperfection range [mm]	[−0.13, 0.16]	[−0.14, 0.23]	[−0.17, 0.21]	[−0.17, 0.21]	[−0.30, 0.30]	[−0.15, 0.19]
Wall thickness [mm]	0.71 ± 0.02	0.70 ± 0.01	0.70 ± 0.01	0.72 ± 0.02	0.72 ± 0.02	0.72 ± 0.02
R/t-Ratio	162	164	164	159	159	159
	Z1W2	**Z2W2**	**Z3W2**	**Z4W2**	**Z5W2**	**Z6W2**
Radius [mm]	114.78 ± 0.10	114.84 ± 0.17	114.80 ± 0.08	114.80 ± 0.08	114.78 ± 0.05	114.82 ± 0.05
Imperfection range [mm]	[−0.23, 0.29]	[−0.41, 0.42]	[−0.13, 0.19]	[−0.16, 0.30]	[−0.13, 0.24]	[−0.13, 0.36]
Wall thickness [mm]	–	0.82 ± 0.01	–	–	–	–
R/t-Ratio	–	140	–	–	–	–
Est. wall thickness [mm]	0.78	–	0.80	0.80	0.78	0.82

all cylinders are dominated by the ±30° layers, which is apparent in the largest circumferential imperfection modes. The largest imperfection modes from the sixth circumferential full wave onwards usually have a ratio of 3:1 between circumferential full waves and axial half waves. This is visualised by the two matrices in the middle of Fig. 5, exemplified on Z2L1 and Z1W2. In direct comparison, the imperfection patterns of the wound shells are more regular than those of the layered ones. The wound cylinders have distinct fourth, sixth and twelfth circumferential modes which may be associated with crossover sections. For the layered cylinders this is not the case. Furthermore, irregularities, such as fibre overlap, caused more irregular imperfection modes.

3.2. Buckling loads

The twelve cylinders were tested on the three test benches as described in Table 2. Tables 5 and 6 list the buckling load achieved in the first test (labelled 'first buckling load') and the highest achieved buckling load of all cylinders in each investigated configuration. In most cases, the buckling load recorded in the first test is also the highest one achieved by any one shell. Notable exceptions to this are only the shells investigated in the first test series, Z1L1 to Z3L1 and Z3W2. If lateral forces were measured, this is also indicated. Additionally, tilt angles and tilt directions immediately before buckling are given. The direction of lateral forces and tilting is described in the cylinder coordinates for each shell. The shells of the first set did not buckle properly during first tests, since the connection to the test platform shifted slightly, resulting in low buckling loads. The connection was improved after the tests with Z1L1 to Z3L1 and Z3W2. This could be a reason for the high lateral forces and tilt angles compared to other tests with fixed connections.

A description of the test results of Z3W2 is presented in [25]. The cylinder Z2L1 was tested 30 times utilising the fixed connection without significant drop in buckling load. As shown in Fig. 7, the buckling load even increased during testing. Between the tenth and eleventh test, the cylinder was slightly realigned, as lateral forces were still applied after retraction. This realignment caused changes in the buckling pattern, as visualised by the curves of the strain gauges in Fig. 8. Changing the boundary condition from clamped to simple support results in significantly lower buckling loads, see Fig. 9. Additionally, the filament-wound shells in particular exhibit a notable decrease in buckling load over several subsequent tests with this type of boundary condition. With exception of the cylinders of the first set, the highest buckling load is achieved for all shells in the first test. After that, it drops slightly and remains at this value with a fixed connection. No significant decrease of axial stiffness is observed over the course of the experiments. The smeared Young's modulus in axial direction of each shell is calculated by using the known dimensions of the shells and the mean of local strains recorded by the strain gauges. Following the guidelines of [32], the strain interval for calculating the stiffness was taken to be (−0.05%, −0.25%) if possible. For the layered shells the estimated smeared Young's modulus is 58.2 ± 1.1 GPa while the shells of the third set exhibit a significantly lower stiffness of 53.2 ± 1.1 GPa.

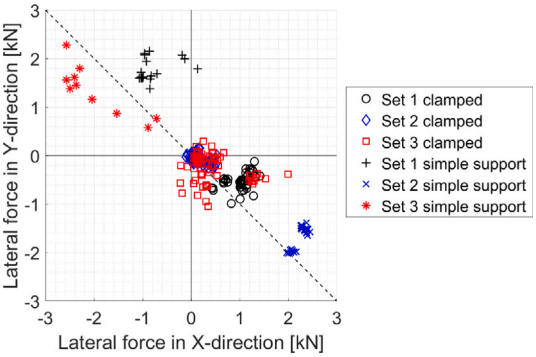

Fig. 6. Measured lateral forces before buckling in the Hexapod coordinate system.

During the first series of tests with shells of set 1 and Z3W2, lateral forces of up to 2.0 kN were recorded before buckling when using the clamped boundary condition and up to 2.9 kN in experiments with the simple support. In all subsequent testing campaigns, shear loads measured before onset of buckling did not exceed 0.8 kN for a clamped upper fixture while the strength of lateral forces remained largely unchanged for the simply supported boundary condition. Furthermore, it is observed that on the Hexapod test rig lateral forces tend to act in the direction of the second or fourth quadrant of the test rigs coordinate system, as shown in Fig. 6. In contrast, during the tests with Z2L2 and Z2W2 on the Galdabini test rig lateral loads are observed acting in the direction of the first and third quadrant of the machine's coordinate system (see Tables 5 and 6).

In tests carried out at the DLR buckling facility, only axial force and displacement were recorded. The highest buckling load was achieved in the first test for each shell with only a small decrease before reaching a plateau in subsequent tests. As described above, when slight realignments were undertaken between tests, in some cases an increase in buckling load was observed. For the shell Z1W2 in the regular clamped configuration, the first buckling load is 67.1 kN with an apparent plateau at 66.0 kN after seven tests. Removing the epoxy layers between fixtures and test rig results in a buckling load of 62.5 kN with a steady decrease over five tests to 61.0 kN, as shown in the upper diagram of Fig. 10. Subsequent tests on the Hexapod deliver buckling loads ranging between the two set ups used at the DLR. While the first buckling load of Z4W2 is nearly identical between the Hexapod and the DLR buckling facility, as illustrated the lower diagram in Fig. 10, for Z5W2 a difference of about 2.5 kN is observed. Furthermore, the first buckling load achieved with the UTM is of similar magnitude to the one reached at the Hexapod. Nevertheless, a significant decrease in buckling load over subsequent tests is only found on the UTM, as exemplified in Fig. 9 on Z2L2 and Z2W2.

3.3. Numerical analysis

The results of the first numerical study, where individual geometric imperfection patterns were applied to shells with four different stacking

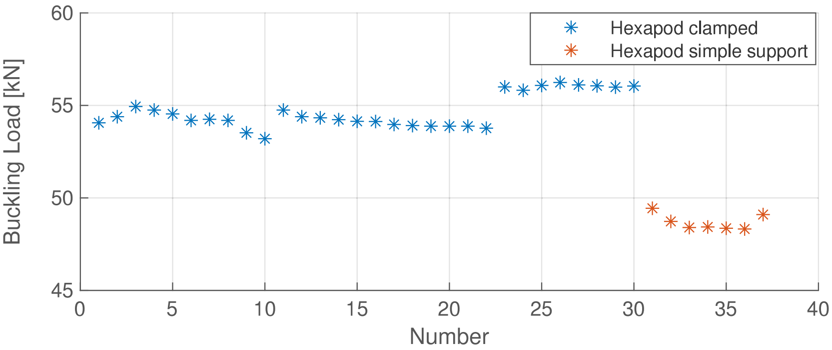

Fig. 7. Buckling loads of Z2L1.

Table 5
Buckling loads of the cylinders of Set 1 and 2.

	Z1L1	Z2L1	Z3L1	Z1L2	Z2L2	Z3L2
First buckling load [kN]	47.17	54.06	49.20	66.26	64.16	63.49
Lateral force [kN]	1.98	1.84	1.48	0.53	0.23	0.18
Lateral force direction	−144.2°	6.4°	−16.5°	0.6°	−140.7°	84.4°
Tilting angle	0.049°	0.017°	0.020°	0.002°	0.004°	0.007°
Tilting direction	25.2°	−79.6°	8.3°	−49.2°	−170.9°	117.3°
Highest buckling load clamped Hexapod [kN]	54.86	56.24	51.51	66.26	64.16	63.49
Lateral force [kN]	1.35	1.22	0.93	0.53	0.23	0.18
Lateral force direction	−41.6°	−32.4°	−36.2°	0.6°	−140.7°	84.4°
Tilting angle	0.008°	0.013°	0.014°	0.002°	0.004°	0.007°
Tilting direction	70.2°	0.2°	5.9°	−49.2°	−170.9°	117.3°
Highest buckling load simple support Hexapod [kN]	51.41	49.44	51.93	55.74	54.26	58.35
Lateral force [kN]	1.82	1.92	1.79	2.91	2.79	2.91
Lateral force direction	113.2°	123.9°	85.8°	−32.8°	146.8°	76.8°
Tilting angle	0.040°	0.036°	0.028°	0.063°	0.043°	0.035°
Tilting direction	61.1°	52.8°	86.0°	−29.5°	−15.5°	−42.4°
Highest buckling load clamped Galdabini [kN]	–	–	–	–	61.35	–
Lateral force [kN]	–	–	–	–	0.23	–
Lateral force direction	–	–	–	–	126.1°	–
Tilting angle	–	–	–	–	0.006°	–
Tilting direction	–	–	–	–	−71.7°	–

Table 6
Buckling loads of the cylinders of Set 3.

	Z1W2	Z2W2	Z3W2	Z4W2	Z5W2	Z6W2
First buckling Load [kN]	67.14	66.25	59.90	64.07	62.15	66.54
Lateral force [kN]	–	0.15	2.03	0.17	0.21	0.72
Lateral force direction	–	−5.5°	−11.1°	27.7°	156.2°	−62.2°
Tilting angle	–	0.002°	0.023°	0.002°	0.005°	0.004°
Tilting direction	–	63.5°	25.4°	−53.7°	114.4°	−66.2°
Highest buckling load clamped Hexapod [kN]	63.70	66.25	59.90	64.07	62.15	66.54
Lateral force [kN]	0.69	0.15	2.03	0.17	0.21	0.72
Lateral force direction	−64.1°	−5.5°	−11.1°	27.7°	156.2°	−62.2°
Tilting angle	0.001°	0.002°	0.023°	0.002°	0.005°	0.004°
Tilting direction	−39.1°	63.5°	25.4°	−53.7°	114.4°	−66.2°
Highest buckling load simple support Hexapod [kN]	–	–	57.88	–	–	60.78
Lateral force [kN]	–	–	2.91	–	–	2.35
Lateral force direction	–	–	141.2°	–	–	150.5°
Tilting angle	–	–	0.038°	–	–	0.040°
Tilting direction	–	–	24.4°	–	–	24.8°
Highest buckling Load clamped Galdabini [kN]	–	63.97	–	–	–	–
Lateral force [kN]	–	0.16	–	–	–	–
Lateral force direction	–	39.8°	–	–	–	–
Tilting angle	–	0.005°	–	–	–	–
Tilting direction	–	−15.3°	–	–	–	–
Highest buckling load DLR [kN]	67.14	–	–	64.20	65.20	–

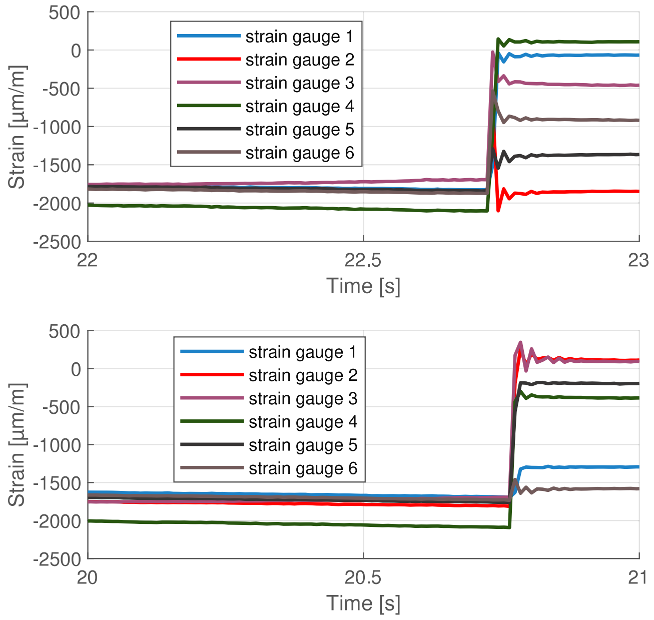

Fig. 8. Measurements of the strain gauges during buckling Z2L1 for test 10 (top) and 11 (bottom).

sequences, are illustrated in Fig. 11. In general, to calculate the buckling loads of the imperfect shells as well as for the later discussed design approaches, non-linear FE-simulations are carried out with the model described in Section 2.3. The perfect buckling loads are estimated via linear Eigenvalue analyses utilising the same FE-model. For the perfect shell, the buckling load changes by about 0.5 kN between different layups. The largest range as well as the largest reduction of buckling load is observed for the imperfection pattern of Z2L2. The remaining shells of the first and second set each exhibit a span of 0.8% to 2.2% between highest and lowest buckling load, with an average load reduction of 2.0% to 3.4% compared to the perfect shell of each stacking sequence. The imperfection patterns of the third set result on average in slightly higher buckling loads while showing notably smaller scatter for different layups than the first two. Load reductions in relation to the perfect shells range from 1.0% to 1.6%. The greatest absolute difference between stacking sequences is 0.8 kN which is observed for Z3W2, while Z4W2 shows the largest relative range with reductions from 1.1% to 2.4%.

In subsequent analyses the individual wall thicknesses and resulting material properties of the different shells are considered. The smeared Young's modulus in axial direction is underestimated by 1.0% to 2.9% for the layered shells. In case of the filament-wound shells an overestimation of 1.7% to 3.7% is observed. Taking into consideration the findings of Schillo [8] that a thin resin-layer remains on the outside of the wound shells after removing the peel-ply, further analyses were carried out. Assuming a mean resin layer thickness of 0.05 mm for the third set and rescaling the material parameters accordingly resulted in overestimating the stiffness by 0.6% to 2.6%.

As described in Section 2.3, different imperfections were iteratively included in the numerical model. The simulation results were compared with the highest experimental buckling loads obtained at the Hexapod test rig with the clamped boundary condition (see Tables 5 and 6). A visualisation of this comparison is given in Fig. 12. For the layered shells tested in the first series of experiments, Z1L1 to Z3L1, there is still a great overestimation of the buckling load by 9.0% to 19.4% when considering all measured imperfection types. The analyses of the second set of cylinders are in good agreement with the test data, deviations ranging from −1.0% to +2.0%. Here, the implementation of lateral forces and tilting of the upper fixture only result in minor changes in the numerically calculated buckling load. Regarding the six filament-wound shells, the buckling loads of the analyses including all measured influence factors are 5.7% to 9.5% higher than the test results. Calculations run without reduced wall-thickness and adjusted material parameters deliver loads up to 17% higher than the experimental data.

Similar sets of simulations were carried out for a simply supported upper fixture. Here, the deviation between test data and analysis exhibits a greater overall scatter. For the first set, buckling loads are overestimated by 10.3% to 16.3% while for the second set of cylinders, the error ranges from −8.5% to +1.0%.

The design loads calculated for nominal specifications and individual shells are summarised in Table 7. In case of the NASA SP-8007 and the SPLA, no significant change is observed when the stacking sequence of the ±30° layers is varied, whereas this variation greatly influences the design load of the LBMI approach. The imperfection amplitudes for the LBMI are 0.15 mm for the first two sets and 0.2 mm for the third set representing average deviation from the perfect shape. To represent the worst measured imperfection shape of each batch, amplitudes of 0.3 mm for the layered and 0.4 mm for the wound shells are chosen (see Table 4). The lowest design loads for this approach are achieved assuming a [90.5°, −30°, +30°, −30°, +30°, 90.5°] layup and are given in Table 7. Using a [90.5°, −30°, +30°]s layup results in the highest design loads which are 45.7 kN for the worst case and 55.1 kN for the average imperfection amplitude of the filament-wound shells.

Assuming the buckling load to be normally distributed, design loads are calculated for reliability levels of 90% and 99% using the SAP. The means and standard deviations of the buckling load distributions of the three sets are, respectively, 63.1 ± 3.1 kN, 63.9 ± 2.8 kN and 67.2 ± 4.9 kN. In Table 7 no design load is given for Z3W2 since the load imperfections observed for this specimen are much larger than for the remaining shells of this set.

4. Discussion

The optical imperfection measurement data showed that the filament-wound shells possess more regular imperfection shapes than the layered ones. At the same time, the average magnitude of form deviations is slightly larger for the filament-wound cylinders, which may be a result of fibre crossings induced by the manufacturing process. From Fig. 11 it is apparent that the stacking sequence of the ±30° layers does have a small influence on the buckling load. Notably, some interaction between geometric imperfection pattern and laminate layup is observed, since the stacking sequence yielding the highest and lowest loads varies even within each of the sets. As the wound shells possess more regular imperfections, a smaller scatter in the simulations is observed for the third set. One conclusion is that the filament-winding process leads to a more consistent quality of the shells and thus to lower scatter in buckling loads. The experimental results support the hypothesis that more regular imperfection patterns, even those with higher imperfection amplitudes, cause less of a reduction in buckling load compared to more irregular ones, such as from fibre overlap. Regarding practical application where buckling is to be avoided, it thus seems preferable to use filament-winding as a manufacturing technique.

According to NASA SP-8007, for validation of high-fidelity models pre-buckling stiffnesses are expected to deviate about ±2% from experimental values while for buckling loads a corridor of about ±5% is given [7]. Based on the small deviation of the shell stiffness between simulation and experiment for all three sets, the methodology and assumptions used to estimate material parameters deliver a good approximation of the real values. However, the consistent underestimation of stiffness for the first two sets hints at potential for optimisation of the numerical model. In filament-wound shells the numerous fibre undulations at crossover sections of tows generally result in a reduction of axial stiffness and buckling load [22,33,34]. As these effects were not considered in the numerical model, an overestimation of stiffness and buckling load was to be expected for the third set. The large difference

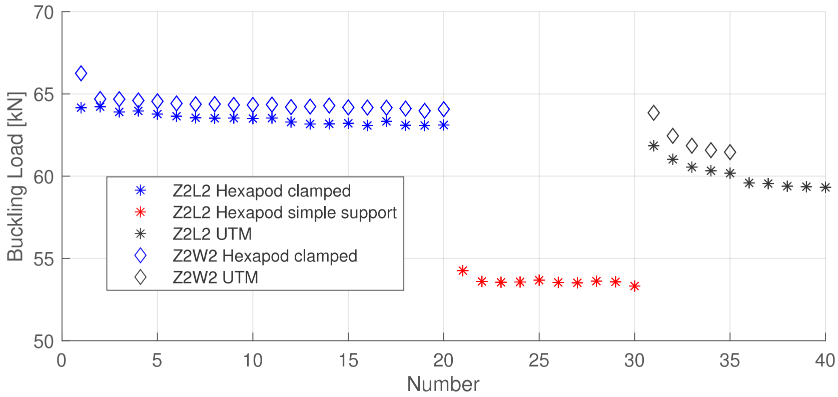

Fig. 9. Buckling loads of Z2L2 and Z2W2.

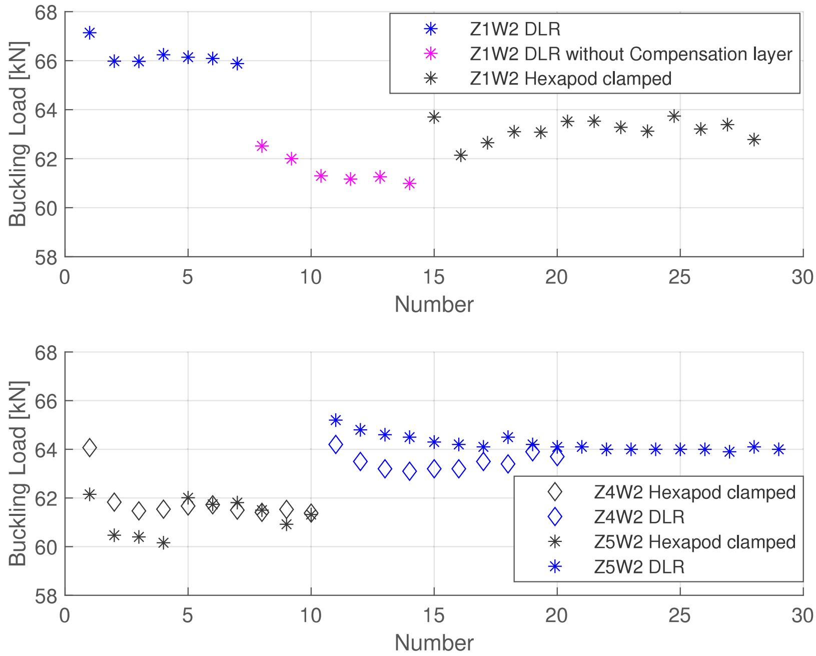

Fig. 10. Buckling loads of Z1W2, Z4W2 and Z5W2.

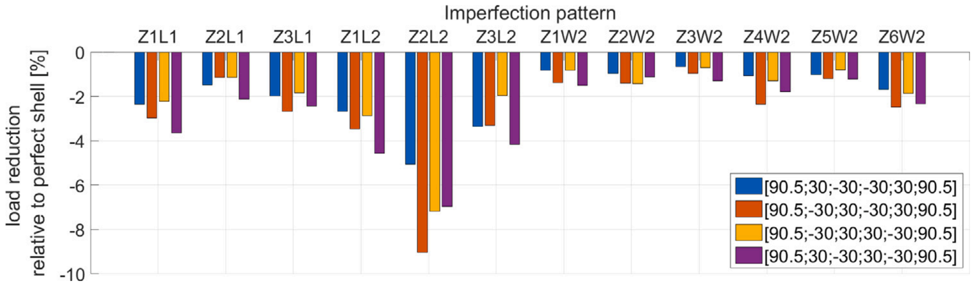

Fig. 11. Comparison of numerical buckling loads for different stacking sequences.

in wall thickness between the first two and the third set points to the existence of a thin layer of leftover resin on the outside of these shells. This layer would affect the photogrammetric measurements, resulting in a greater wall thickness that is partially not contributing to the load carrying capacity. Indeed, accounting for a thin resin layer reduces the discrepancy between numerical and experimental results. This assumption is supported by Schillo [8].

The difference between simulated buckling loads and the values observed in tests is greatest for shells tested in the first series of experiments (Z1L1 to Z3L1 and Z3W2). The stepwise expansion of the analyses for these four specimens also most prominently shows the influence of measured lateral forces and tilting of the shell edge, particularly for Z3W2. The large discrepancy in buckling load in those cases is most likely based on neglection of imperfections in load introduction and boundary conditions. Since these shells were the first ones to be tested, the aforementioned shift in the connection to the test rig represents an unquantified factor that possibly influences the buckling load. Thus, it stands to conclude that thorough documentation

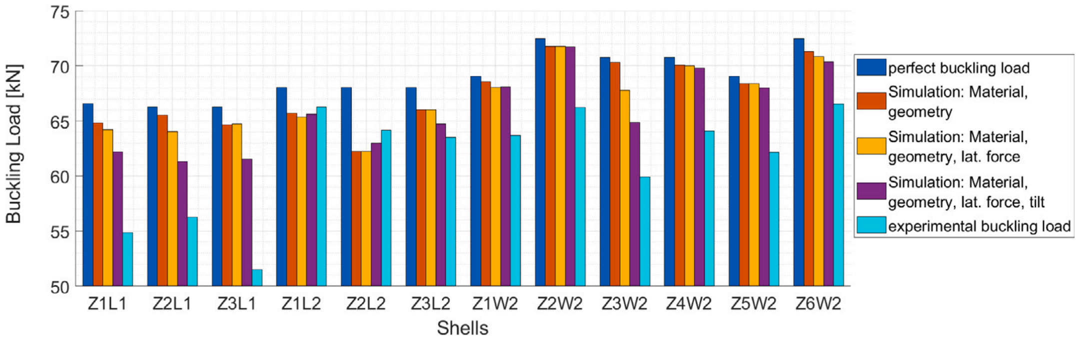

Fig. 12. Numerical buckling loads for different model setups.

Table 7
Design loads for different design approaches.

	Nominal	Z1L1	Z2L1	Z3L1	Z1L2	Z2L2	Z3L2
NASA SP-8007 [kN]	46.8						
SPLA [kN]	65.9	59.0	58.8	58.8	60.3	60.3	60.3
LBMI ($\xi = [0.3, 0.15]$ mm) [kN]	[36.7, 43.8]						
SAP (reliability 0.99) [kN]	–	55.9	55.9	55.9	57.5	57.5	57.5
SAP (reliability 0.90) [kN]	–	59.1	59.1	59.1	60.4	60.4	60.4
	Nominal	Z1W2	Z2W2	Z3W2	Z4W2	Z5W2	Z6W2
NASA SP-8007 [kN]	46.8						
SPLA [kN]	65.9	61.5	64.6	63.0	63.0	61.5	64.6
LBMI ($\xi = [0.4, 0.2]$ mm) [kN]	[38.2, 43.0]						
SAP (reliability 0.99) [kN]	–	55.8	55.8	–	55.8	55.8	55.8
SAP (reliability 0.90) [kN]	–	60.9	60.9	–	60.9	60.9	60.9

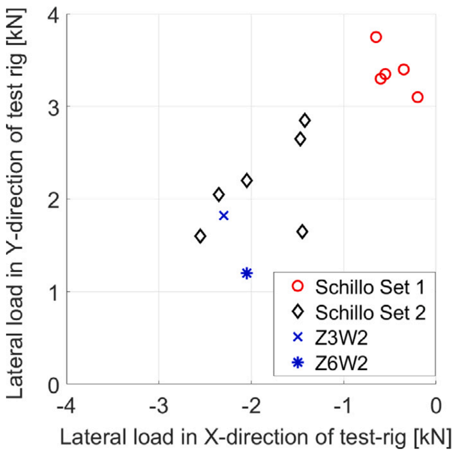

Fig. 13. Comparison of lateral forces from [8] with Z3W2 and Z6W2.

of test procedures and results is essential for development, validation and assessment of design approaches based on such experimental data.

A direct comparison of the experiments carried out in this work with those in [8] is possible for the tests of Z3W2 and Z6W2 with a simply supported boundary condition. For these, good agreement between the results of Schillo and the current study is observed. The achieved buckling loads of 57.9 kN and 60.8 kN fall well within the sample distribution of Schillo, which is given as 59.3 ± 2.4 kN in [6]. Similarly, the measured lateral forces for these experiments are comparable, as illustrated in Fig. 13. The experimental results presented in this work show a significantly larger tilt for buckling tests with a simple support as compared to using the clamped boundary condition. For both Z3W2 and Z6W2, the buckling load decreased by 20%–30% over the course of four subsequent tests with the simple support which points to internal damage and degradation being induced by this kind of test rig boundary condition. For the layered shells the decrease in buckling load is only about 5% when using the simply supported boundary condition. This leads to hypothesise that shells manufactured in a layer-by-layer process offer better reproducibility in buckling experiments with unknown or not fully characterised boundary conditions.

Comparing the recorded buckling loads from the different test rigs and boundary conditions, it is apparent that allowing for shifting or tilting of one shell edge, e.g. in a simply supported set-up or by leaving out the epoxy layers between specimen clamping and test rig, leads to significantly lower buckling loads in addition to the aforementioned degradation.

Among the design approaches considered, only the NASA SP-8007 and the LBMI approach are consistently conservative. The LBMI approach is the only one to exhibit high sensitivity to variation of the stacking sequence with results scattering by up to 22%. Excluding the first test series, the SPLA delivers the most accurate prediction of buckling loads for the true wall thickness and material parameters of each specimen. Applying this design approach to nominal data results in overestimating the buckling load in multiple cases. A similar observation was made in [6]. Since the SPLA is usually categorised as a deterministic approach that does not require measurement data [3,12], the results for nominal geometry should be primarily considered. Two reasons for the low design loads of the SAP for a reliability level of 0.99 are identified. Firstly, the sample sizes considered in this study are rather small, possibly leading to an inaccurate stochastic description of different model parameters. Secondly, correlations between global wall thickness and material properties, both of which affect the buckling load, have been neglected. Thus, it is viable to assume the calculated standard deviations are larger than the true scatter with respect to the influence factors considered.

The experimental data show that variation of the test rig may cause differences in buckling loads of similar magnitude as the scatter between different specimens tested in the same set up, as well as load reduction caused by individual known influence factors. However, the exemplary applied design approaches are all sufficiently conservative to account for the test rig influence of the shell configurations investigated in this study.

5. Conclusion

In this work, 12 cylindrical CFRP-shells were investigated by performing imperfection measurements and buckling tests in axial compression. While geometric specification, layup and material were identical for all shells, two different fabrication processes were used. Buckling experiments were carried out on three different test rigs, on two of which two different sets of boundary conditions were implemented. During these tests, occurring lateral forces and tilting of the upper fixture of the shells were measured, providing additional data on the influence of the test setup on the buckling behaviour. Several shells were also tested on different test rigs in succession to investigate the effects of the testing machine on the buckling load. The experimental results show that the test rig influence on the buckling load is of similar magnitude as the one of other commonly known influence factors. Generally, UTM are found to be suitable for buckling tests, despite the restrictions on the size of specimens. However, the lower stiffness of such test rigs may result in load deviations, thus inducing degradation in the shells. Similarly, utilising test rig boundary conditions permitting free tilting of the shell also results in possible degradation of the cylinders as well as significantly lower buckling loads compared to fully clamped boundary conditions.

It could be shown that the fabrication method, layer-by-layer or filament-winding, does have an influence on the imperfection pattern and stiffness of a shell as well as on the suitability for use with different test rig boundary conditions. While filament-wound shells exhibit a more regular imperfection pattern and smaller sensitivity to a variation of the stacking sequence, the layered shells have on average a smaller magnitude of geometric imperfections. In addition, layered shells show less degradation under test rig boundary conditions that allow for shifting or tilting, e.g. a simply supported set-up.

In the present work only shells with the same dimensions and one specific laminate were investigated. However, it is known that shells with larger R/t-ratios tend to exhibit stronger imperfection sensitivity, as shown e.g. in [35]. Hence, it is to be expected that the effects observed in this study would be even more pronounced. Additionally, it has been shown in the past that different laminate layups can greatly influence the imperfection sensitivity of a shell, e.g. in [36]. Thus, it is recommended for further research to be carried out on this topic with cylinders of different R/t-ratios or laminate layups.

CRediT authorship contribution statement

Tobias S. Hartwich: Conceptualization, Methodology, Investigation, Visualization Writing – original draft. **Stefan Panek:** Formal analysis, Investigation, Visualization, Writing – original draft. **Dirk Wilckens:** Investigation, Visualization, Writing – original draft. **Matthias Bock:** Resources, Writing – original draft. **Dieter Krause:** Supervision, Project administration, Funding acquisition, Writing – review & editing.

Declaration of competing interest

The authors declare that they have no known competing financial interests or personal relationships that could have appeared to influence the work reported in this paper.

Data availability

Data will be made available on request.

Acknowledgements

This research was funded by German Research Foundation (DFG) via the project *Zuverlässigkeitsbasierte Auslegung unversteifter CFK-Zylinderschalen unter Material- und Strukturunsicherheiten*. The Hexapod was also funded by the DFG.

Finally, we would like to acknowledge Dirk Röstermundt, who passed away too soon, for manufacturing the cylinders and his valuable contribution to the success of the project mentioned above.

References

[1] Singer J, Arbocz J, Weller T. Buckling experiments: Experimental methods in buckling of thin-walled structures. Chichester: Wiley; 2002.

[2] Arbocz J, Hilburger MW. Toward a probabilistic preliminary design criterion for buckling critical composite shells. AIAA J 2005;43(8):1823–7.

[3] Hühne C, Rolfes R, Breitbach E, Teßmer J. Robust design of composite cylindrical shells under axial compression — Simulation and validation. Thin-Walled Struct 2008;46(7–9):947–62.

[4] Degenhardt R, Kling A, Bethge A, Orf J, Kärger L, Zimmermann R, Rohwer K, Calvi A. Investigations on imperfection sensitivity and deduction of improved knock-down factors for unstiffened CFRP cylindrical shells. Compos Struct 2010;92(8):1939–46.

[5] Takano A. Statistical knockdown factors of buckling anisotropic cylinders under axial compression. J Appl Mech 2012;79(5).

[6] Schillo C, Kriegesmann B, Krause D. Reliability based calibration of safety factors for unstiffened cylindrical composite shells. Compos Struct 2017;168:798–812.

[7] Hilburger MW. NASA-SP-8007-2020/REV 2: Buckling of thin-walled circular cylinders. 2020.

[8] Schillo C, Röstermundt D, Krause D. Experimental and numerical study on the influence of imperfections on the buckling load of unstiffened CFRP shells. Compos Struct 2015;131:128–38.

[9] Kriegesmann B, Jansen EL, Rolfes R. Design of cylindrical shells using the Single Perturbation Load Approach – Potentials and application limits. Thin-Walled Struct 2016;108:369–80.

[10] Bolotin VV. Statistical method in the nonlinear theory of elastic shell. 1962.

[11] Hilburger MW, Starnes JH. Effects of imperfections on the buckling response of compression-loaded composite shells. Int J Non-Linear Mech 2002;37:623–43, Stability and Vibration in Thin-Walled Structures.

[12] Wagner H, Hühne C, Elishakoff I. Probabilistic and deterministic lower-bound design benchmarks for cylindrical shells under axial compression. Thin-Walled Struct 2020;146:106451.

[13] Meyer-Piening H-R, Farshad M, Geier B, Zimmermann R. Buckling loads of CFRP composite cylinders under combined axial and torsion loading – experiments and computations. Compos Struct 2001;53(4):427–35.

[14] Bisagni C. Composite cylindrical shells under static and dynamic axial loading: An experimental campaign. Prog Aerosp Sci 2015;78:107–15.

[15] Franzoni F, Odermann F, Lanbans E, Bisagni C, Andrés Arbelo M, Degenhardt R. Experimental validation of the vibration correlation technique robustness to predict buckling of unstiffened composite cylindrical shells. Compos Struct 2019;224:111107.

[16] Bisagni C, Cordisco P. An experimental investigation into the buckling and post-buckling of CFRP shells under combined axial and torsion loading. Compos Struct 2003;60(4):391–402.

[17] Elghazouli AY, Chryssanthopoulos MK, Esong IE. Buckling of woven GFRP cylinders under concentric and eccentric compression. Compos Struct 1999;45(1):13–27.

[18] Schmidt H, Winterstetter T. Buckling interaction strength of cylindrical steel shells under axial compression and torsion. In: Advances in steel structures (ICASS '99), Vol. II. Elsevier; 1999, p. 597–604.

[19] Takano A. Buckling experiment on anisotropic long and short cylinders. Adv Technol Innov 2016;1(1).

[20] Skukis E, Ozolins O, Kalnins K, Arbelo MA. Experimental test for estimation of buckling load on unstiffened cylindrical shells by vibration correlation technique. Procedia Eng 2017;172:1023–30.

[21] Taheri-Behrooz F, Omidi M, Shokrieh MM. Experimental and numerical investigation of buckling behavior of composite cylinders with cutout. Thin-Walled Struct 2017;116:136–44.

[22] Hipp P, Jensen D. Design and analysis of filament-wound cylinders in compression. In: 33rd structures, structural dynamics and materials conference. Reston, Virigina: American Institute of Aeronautics and Astronautics; 1992, p. 2442–52.

[23] Castro SGP, Zimmermann R, Arbelo MA, Khakimova R, Hilburger MW, Degenhardt R. Geometric imperfections and lower-bound methods used to calculate knock-down factors for axially compressed composite cylindrical shells. Thin-Walled Struct 2014;74:118–32.

[24] Kriegesmann B, Rolfes R, Hühne C, Kling A. Fast probabilistic design procedure for axially compressed composite cylinders. Compos Struct 2011;93:3140–9.

[25] Hartwich TS, Krause D. The influence of geometric imperfections of different tolerance levels on the buckling load of unstiffened CFRP cylindirical shells. In: 22th international conference on composite materials (ICCM22). 11-16 August 2019, p. 4502–11..

[26] Plaumann B, Rasmussen O, Krause D. System analysis and synthesis for the dimensioning of variant lightweight cabin interior. In: 54th AIAA/ASME/ASCE/AHS/ASC structures, structural dynamics, and materials conference. 2013.

[27] Hartwich TS, Völkl H, Wartzack S, Krause D. Designing lightweight structures under consideration of material and structure uncertainties on different levels of the building block approach. In: Proceedings of the 31st symposium design for X (DFX2020). The Design Society; 2020, p. 121–30.

[28] Hexcel. HexPly 8552 product data sheet. 2020.

[29] Khakimova R, Wilckens D, Reichardt J, Zimmermann R, Degenhardt R. Buckling of axially compressed CFRP truncated cones: Experimental and numerical investigation. Compos Struct 2016;146:232–47.

[30] Sosa EM, Godoy LA, Croll JGA. Computation of lower-bound elastic buckling loads using general-purpose finite element codes. Comput Struct 2006;84:1934–45.

[31] Meurer A, Kriegesmann B, Dannert M, Rolfes R. Probabilistic perturbation load approach for designing axially compressed cylindrical shells. Thin-Walled Struct 2016;107:648–56.

[32] EN ISO 14126:1999: Fibre-reinforced plastic composites - Determination of compressive properties in the in-plane direction. DIN German Institute for Standardization; 2000.

[33] Hahn HT, Jensen DW, Claus SJ, Pai SP, Hipp PA. NASA/CR-195125 - structural design criteria for filament-wound composite shells. 1994.

[34] Pai SP, Jensen DW. Influence of fiber undulations on buckling of thin filament-wound cylinders in axial compression. J Aerosp Eng 2001;14(01):12–20.

[35] Takano A, Kitamura R, Masai T, Bao J. Buckling test of composite cylindrical shells with large radius thickness ratio. Appl Sci 2021;11(2):854.

[36] Geier B, Meyer-Piening H, Zimmermann R. On the influence of laminate stacking on buckling of composite cylindrical shells subjected to axial compression. Compos Struct 2002;55:467–74.